Temperature dependence of hypersound attenuation in silica films via picosecond acoustics

A. Huynh,[1,*] E. Péronne,[1] C. Gingreau,[1] X. Lafosse,[2] A. Lemaître,[2] B. Perrin,[1] R. Vacher,[3] B. Rufflé,[3] and M. Foret[3]
[1]*Sorbonne Universités, CNRS-UPMC Univ. Paris 06, UMR 7588, Institut des Nanosciences de Paris, F-75005 Paris, France*
[2]*Centre de Nanosciences et de Nanotechnologies, CNRS, Univ. Paris-Sud, Université Paris-Saclay, C2N-Marcoussis, 91460 Marcoussis, France*
[3]*L2C, University of Montpellier, CNRS, Montpellier, France*

(Received 18 May 2017; revised manuscript received 16 October 2017; published 15 November 2017)

We report picosecond acoustic measurements of longitudinal sound dispersion and attenuation in an amorphous SiO_2 layer at temperatures from 20 to 300 K over frequencies ranging from about 40 to 200 GHz. The sample is a radio frequency cathodic sputtered silica layer grown on a sapphire substrate with an aluminum film transducer deposited on top. Acoustic attenuation is evaluated from the simultaneous analysis of three successive echoes using transfer matrix calculation. Results are found to follow rather well a model combining coupling to thermally activated relaxations of structural defects and interactions with thermal vibrations. This leads to a nontrivial variation of the attenuation coefficient with frequency and temperature. The number density of relaxing defects in the SiO_2 layer is found to be slightly higher than that in bulk v-SiO_2. In contrast, similar anharmonic contribution to acoustic absorption is observed in both systems. The velocity variations are also measured and are compared to the dynamical velocity changes deduced from the sound attenuation.

DOI: 10.1103/PhysRevB.96.174206

I. INTRODUCTION

Thin films of amorphous silicon dioxide (SiO_2) are key materials for a variety of applications that range from insulating layers in integrated circuits to overlays for surface acoustic wave (SAW) devices or supports for metal nanoparticles in sensors. The physical properties of the films are often crucial for the performances of the aforementioned applications. It is, however, empirically known that properties of SiO_2-films may considerably vary with preparation details. For instance, the quality factor of SAW resonators is observed to vary with deposition temperature of the SiO_2 overlay due to excess acoustic loss [1]. Deposited SiO_2 layers are also key materials for some precision experiments in which reduction of thermal noise is of crucial importance. The latter arises in part from internal friction within the material forming the resonator [2]. For instance, recent work has revealed that losses in the optical coating (SiO_2/Ta_2O_5 stack) of resonant-mass detectors for gravitational waves have a large contribution to the overall thermal noise [3,4]. It is therefore of fundamental interest to investigate the dissipative mechanisms at the origin of acoustic losses in amorphous dielectric layers and in particular to compare them to those of the bulk material, including the prototypical vitreous silica v-SiO_2.

Several damping mechanisms have been identified in glasses. A major one is assigned to the interaction of sound with the motion of structural entities, called *defects*. Thermally activated relaxation (TAR) processes associated to the defects give rise to an absorption peak at ultrasonic frequencies and below. The latter occurs in the interval 30 to 70 K for v-SiO_2 [5–7]. The frequency dependence of the resulting acoustic attenuation α at any given temperature T may be described in terms of the well-known Debye equation:

$$\alpha(\omega,T) \propto \int G(\tau,T)\frac{\omega^2\tau}{1+\omega^2\tau^2}d\tau, \qquad (1)$$

where G describes the distribution of the relaxation times τ of the defects at T. A good description of absorption data is generally obtained assuming thermal activation in asymmetric double-well systems, the asymmetry being associated to quenched spatial disorder [8]. Regardless of the form of the distribution G, Eq. (1) always gives an attenuation whose frequency dependence is slower than quadratically. As in defect-free single crystals, sound damping originating from anharmonic interactions with the thermally excited phonons is also anticipated in glasses [9] and quasicrystals [10]. In the Akhiezer treatment [11], the sound wave perturbs the phonon frequencies and thus the phonon populations of the thermal bath, which return to equilibrium within the mean thermal lifetime τ_{th} of the dominant vibrations. The relaxation is most efficient for acoustic frequencies ω for which $\omega\tau_{th} \simeq 1$. As τ_{th} is short it ought to contribute to acoustic damping at high ω. An estimate of the relative contribution to sound attenuation in vitreous silica of TAR and Akhiezer mechanism has been provided quite recently in Ref. [12] as part of Brillouin-scattering measurements. Below 10 K and at still lower T, attenuation is produced by interaction of sound with tunneling motions of entities also in asymmetric double wells [13,14]. Those tunneling systems give rise to low-energy states which determine the vibrational dynamics of glasses at low T.

At extremely high frequency, nearing terahertz (THz) range, an ultimate damping mechanism is inferred from the low-T universal plateau in thermal conductivity of glasses [15]. The latter could arise from Rayleigh type scattering by disorder or resonant coupling to the excess modes manifested by the boson peak. Both mechanisms should give rise to a dramatic increase of α with frequency. A strong damping behavior, $\alpha \propto \omega^4$, has been indeed evidenced beyond $\sim$1 THz in few glasses [16–19] (other than silica) owing to advances in Brillouin scattering of x rays [20,21].

Much efforts have been made recently to explore the onset of the ω^4 law over the anharmonicity damping in SiO_2 layers using the great potential of ultrafast acoustic techniques [26,27,29,31–33]. However, it could not be observed until now. Figure 1 illustrates the available attenuation results at

*Corresponding author: agnes.huynh@insp.jussieu.fr

 ©2017 American Physical Society

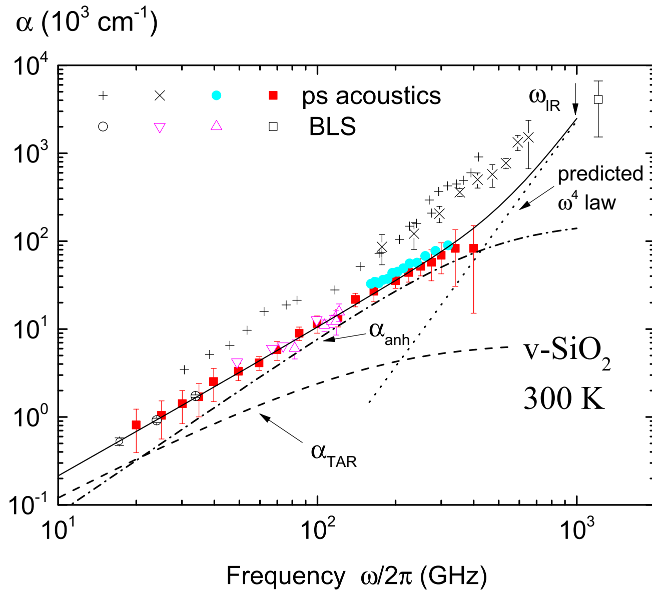

FIG. 1. Collection of energy attenuation coefficient for LA waves in v-SiO_2 at 300 K deduced from different spectroscopies: visible Brillouin light scattering (BLS) results [22] (○), ultraviolet BLS ones (▽ [23,24] and △ [25]) and ps acoustics results in SiO_2 layers by Ayrinhac *et al.* [26] (●) and Klieber *et al.* [27] (■) as well as the early data from Zhu *et al.* [28] (+) and the high-frequency ones from Wen *et al.* [29] (×), which both seem overestimated. The arrow indicates the Ioffe-Regel limit for LA waves from Ref. [17]. The point above the Ioffe-Regel frequency ω_{IR} is from Brillouin x-ray scattering experiment [20]. The solid line is the estimated sum of TAR (dashed line) and anharmonicity (dash-dot line) contributions plus the predicted ω^4 law [30] (dotted line) as explained in text.

hypersonic frequencies which were acquired at room T. Data at low frequency obtained by Brillouin light scattering (BLS) in the visible [22] and ultraviolet [23–25] regions of the spectrum are shown as opened markers. Following the work of Vacher *et al.* [12], one can anticipate the contributions of the above mentioned TAR and anharmonicity mechanisms shown as dashed and dash-dot lines, respectively. Some of the picosecond acoustics results [26,27] remarkably fit the expectation from $(\alpha_{TAR} + \alpha_{anh})$ up to about 300 GHz. This suggests that the damping model as detailed in Ref. [12] is working well even above the BLS frequencies. We also consider in Fig. 1 the data from the historical experiment by Zhu *et al.* [28], the very first of its kind, albeit the associated results (like those from Ref. [29]) appear now clearly overestimated in light of the overall results. Finally, the dotted line in Fig. 1 is a quantitative prediction from the soft potential model [30], the arrow indicating the anticipated Ioffe-Regel limit for LA waves from Ref. [17]. The solid line represents the whole damping which is therefore expected at room T. One immediate idea to test the overall scenario would be to perform experiments at lower temperatures. On cooling, the TAR contribution is expected to prevail against anharmonicity until sufficiently high frequencies are reached. Then by further increasing frequency, as the ω^4 law should be T independent, it should become dominant as T is decreased reducing the anharmonicity damping. However, no significant T-dependence of phonon attenuation was found over the range 30–440 GHz in the seminal work by Maris and co-workers [28].

In this work, we reinvestigate sound dispersion and attenuation in a SiO_2 layer as a function of temperature over the range 20–300 K by ps acoustics. We use a pump-probe technique, analog to that in Ref. [28] with a broadband pulse centered at the intermediate frequency of 120 GHz. The hypersound pulse generated by a pump laser pulse travels back and forth through the silica layer sandwiched between a thin metallic film and a substrate. Attenuation is evaluated from an analysis of the whole acoustic signal based on a mismatch model including an effective law for the ω dependence of α in the SiO_2 layer. Section II describes the samples used and explains the experimental methods. The variations of sound dispersion and attenuation as a function of T found for the SiO_2 layer are presented in Sec. III. They are discussed in terms of TAR and anharmonicity mechanisms. The number density of TAR defects in the SiO_2 layer can be compared to the one of bulk v-SiO_2. Section IV concludes the paper.

II. MATERIAL AND METHODS

A. Experimental setup

Sound attenuation in amorphous SiO_2 layers is investigated by means of picosecond acoustics. The method is based on the decay analysis of acoustic echoes which go back and forth through a silica layer. The sample is a silica layer grown on a sapphire substrate with an aluminum thin film transducer deposited on top as sketched in the inset of Fig. 2. The set-up is based on a femtosecond Ti:sapphire mode-locked laser providing 80-fs pulses (200 fs pulses incoming on the sample) and operating at 770 nm with a repetition rate of 80 MHz.

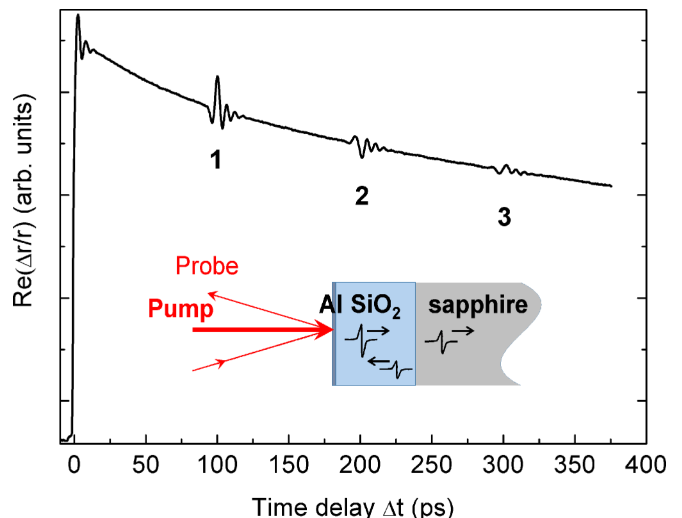

FIG. 2. Transient change of reflectivity (real part) at 45 K as a function of time delay (sputtered-SiO_2 sample). The three echoes, labeled according to their number of round trip, appear on top of a slow relaxation. A schematic sketch of the experiment is shown in inset: the pump pulse is absorbed by the Al film; an acoustic pulse is generated, and propagates through the silica layer as suggested by the arrow; the pulse is partly reflected at SiO_2/sapphire interface and returns to the Al film in which it is detected by the probe pulse.

Each pump laser pulse, focused on the Al film, causes it to rapidly heat. As a result, a strain wave packet is launched into the sample and propagates through the SiO_2 layer. The strain wave is mainly longitudinal as the pump beam is focused over a spot whose diameter is large (about 60-μm wide) compared to the thinness of the Al film (about 20-nm thick). The strain pulse is partly reflected at the SiO_2/sapphire interface. On returning to the Al layer, the strain pulse induces free surface and SiO_2 interface displacements as well as local modification of the Al optical constants. Both effects lead to a transient change of the reflectivity Δr, $r = \rho e^{i\phi}$ being the reflection coefficient of the electric field. The changes of amplitude and phase ($\Delta\rho$ and $\Delta\phi$, respectively) can be measured thanks to a Sagnac interferometer [10], which is particularly insensitive to low frequency noise induced by its mechanical components. The pump is modulated at 1 MHz to allow synchronous detection through a lock-in amplifier and reach a sensitivity better than 10^{-6}.

The sample is mounted in a He continuous-flow cryostat to carry out the measurements from 15 to 300 K. Because of the low thermal conductivity of v-SiO_2, the optical power has been set in order to avoid a steady-state heating of the sample. Practically, we checked that the measured echoes scale linearly with pump and probe power. Typical powers are few tens of milliwatt for the pump and 1-mW 2-mW for the probe. Both beams are focused to a spot diameter of 60-μm on the sample surface.

A typical $\frac{\Delta\rho}{\rho}$ signal measured at 45 K is shown in Fig. 2. The absorption of the pump pulse in the Al film gives rise to the sudden increase in the signal at $\Delta t = 0$ due to the rapid increase of the metallic film temperature. At later time delays, three transient features are recorded on top of a slow decaying background. The latter is the sign of the Al film cooling as heat flows away from the detection area. The subtraction of this background leaves a series of n acoustic echoes, shown in Fig. 3 as black dots, corresponding to the strain pulse detection in the Al film after propagating back and forth n times through the SiO_2 layer. Each echo is labeled according to its number of round trip n. For thin Al films, the spectral content of the strain pulse is mainly set by the film thickness [28,34]. It extends from about 40 to 200 GHz as shown in Fig. 3(b). Studying the changes of shape of the successive echoes allows to evaluate the sound-attenuation coefficient of the SiO_2 layer within the frequency band of the pulse.

B. Samples

The physical characteristics of deposited amorphous SiO_2 layers can be, in practice, different from those of bulk fused silica, depending on deposition techniques and growth conditions [35,36]. Here, the SiO_2 layer is prepared by the reactive radio-frequency (RF) magnetron sputtering technique. Our first stage has been to optimize the deposition parameters so that properties (as density, refractive index and sound velocity) of the produced SiO_2 layer resemble those of thermally grown SiO_2 on silicon taken as a reference. The selected deposition conditions are summarized in Table I. The sapphire surface has to be cleaned by hydrogen plasma etching before SiO_2 deposition. The thickness of the selected SiO_2 layer evaluated by ellipsometry is $d = 281(2)$ nm. The OH content in the SiO_2 layer is expected to be the one of the target, i.e., $\leqslant$20 ppm.

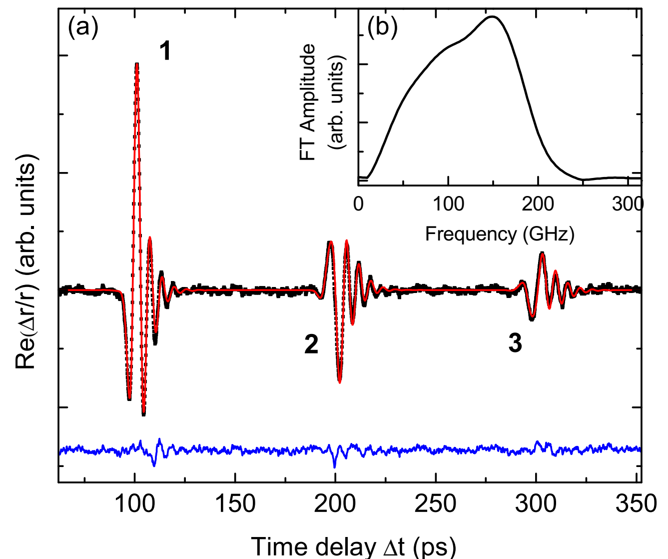

FIG. 3. (a) Transient change of reflectivity (real part) at 45 K as a function of time delay, after subtraction of an ad-hoc smooth thermal background (•) to enhance the echoes (sputtered-SiO_2 sample). Superimposed, typical fit (red line) of the three first acoustic echoes. Bottom curve: difference between the experimental signal and the fit (residual), shifted for clarity. (b) Fourier transform amplitude of the first echo.

Finally, the layer is capped by an evaporated thin Al film of nominal thickness $l = 20$ nm. Aluminum is chosen for short optical skin depth enabling broadband detection. Its large linear dilatation coefficient induces also efficient photothermal transduction. Moreover its acoustic impedance is close to the silica one thus reducing reflection at Al/SiO_2 interface. Sapphire, in contrast, is chosen on account of its high acoustic impedance as compared to silica one. This results in the large strain pulse reflection, $r_{ac} \simeq 0.53$, at SiO_2/sapphire interface.

To provide a benchmark sample, we also produce a thermally grown SiO_2 layer by dry thermal oxidation of silicon. The oxidation is performed at a substrate temperature of 1100 °C in a flow of O_2 gas during about 8 hours. This results in a SiO_2 layer about 400(10)-nm thick. An Al film 20-nm thick is evaporated on top as above. This sample is referred to as *dryox* hereafter.

C. Data analysis

We are interested in computing the acoustic echo signal which is associated to the propagating part of the photothermal strain generated in the Al film. The signal is analyzed in

TABLE I. SiO_2 film deposition parameters.

Target	fused quartz
Gas composition	50% Ar + 50% O_2
Sputtering pressure	0.2 Pa
RF power	1.1 W/cm^2
Substrate temperature	300 °C
Deposition rate	0.115 μm/h

the time domain with the help of an acoustic impedance mismatch model as discussed in the forthcoming paragraph. As introduced in Sec. I, TAR and anharmonicity mechanisms are expected to damp the acoustic pulse in the SiO_2 layer. Both mechanisms can be described in terms of relaxation processes. However, these have different ω and T dependencies. We thus employ an *ad hoc* power law for the frequency dependence of sound attenuation in the layer, $\alpha(\omega,T) = \alpha_0(T)\omega^{p(T)}$ in order to represent the effective sound damping over the ω band of the pulse [7]. The exponent should be T-dependent, while satisfying $p(T) \leqslant 2$. In the following, α denotes the rate of attenuation of the energy in the acoustic pulse, per unit distance.

Strain-pulse generation from thermal expansion of metallic films upon light-pulse absorption is well-documented [37,38]. The photothermal generation is treated as an impulsive surface loading with a Gaussian profile $\sigma(t,z=0) \propto e^{-t^2/\delta^2}$, whose typical duration is characterized by δ, z being the coordinate perpendicular to the sample. Free boundary conditions at the Al free-surface and displacement-stress continuity at the other two interfaces are assumed. Let us also consider the sapphire substrate as an infinite medium. Based on an acoustic impedance mismatch model, one can calculate the Al free-surface displacement, $u_0(\omega)$, from the transient surface stress $\sigma(t,z=0)$:

$$u_0(\omega) = \frac{A(\omega)e^{-iq_m l} + B(\omega)e^{iq_m l}}{A(\omega)e^{-iq_m l} - B(\omega)e^{iq_m l}} \frac{\sigma(\omega,z=0)}{iZ_m v_m q_m} \tag{2}$$

with

$$\begin{aligned} A(\omega) = &\left[1 + \frac{Z_g}{Z_m}\left(1 + \frac{\alpha}{2iq_g}\right) + \frac{Z_s}{Z_g}\left(1 + \frac{\alpha}{2iq_g}\right)^{-1} + \frac{Z_s}{Z_m}\right] e^{-iq_g d} e^{\frac{-\alpha d}{2}} \\ &+ \left[1 - \frac{Z_g}{Z_m}\left(1 + \frac{\alpha}{2iq_g}\right) - \frac{Z_s}{Z_g}\left(1 + \frac{\alpha}{2iq_g}\right)^{-1} + \frac{Z_s}{Z_m}\right] e^{iq_g d} e^{\frac{\alpha d}{2}}, \end{aligned} \tag{3}$$

$$\begin{aligned} B(\omega) = &\left[1 - \frac{Z_g}{Z_m}\left(1 + \frac{\alpha}{2iq_g}\right) + \frac{Z_s}{Z_g}\left(1 + \frac{\alpha}{2iq_g}\right)^{-1} - \frac{Z_s}{Z_m}\right] e^{-iq_g d} e^{\frac{-\alpha d}{2}} \\ &+ \left[1 + \frac{Z_g}{Z_m}\left(1 + \frac{\alpha}{2iq_g}\right) - \frac{Z_s}{Z_g}\left(1 + \frac{\alpha}{2iq_g}\right)^{-1} - \frac{Z_s}{Z_m}\right] e^{iq_g d} e^{\frac{\alpha d}{2}}, \end{aligned} \tag{4}$$

where v, q, and Z are sound velocity, wave number and impedance in the medium specified in subscript (m stands for Al metal, g for SiO_2 glass and s for sapphire substrate); l and d denote the thicknesses of the metallic Al film and the glassy SiO_2 layer, respectively.

Two distinct processes act on the reflection coefficient of the multilayer system: first, the elastic strain slightly modifies the optical properties within the layers and, second, the interfaces of the sample are displaced by the acoustic field [39,40]. However, as most of the probe light is either reflected by or absorbed in the capping metallic layer, the photoelastic response from both the SiO_2 layer and the substrate can be neglected. Finally (see details in Ref. [41]), the real part of the reflectivity changes are dominated by the Al-film thickness changes alone, and may be given by

$$\frac{\Delta\rho(\omega)}{\rho} = \mathrm{Re}\left\{2ik_0\left(\varepsilon_m + \frac{1}{2}\frac{\partial\varepsilon_m}{\partial\eta}\right)\frac{a_m b_m}{n_0 a_0 b_0}[\cos(q_m l) - 1]u_0(\omega)\right\}, \tag{5}$$

where the subscript 0 stands for air; k is the electromagnetic field wave number; a and b are the amplitudes of incident and reflected electromagnetic fields, respectively; ε is the dielectric constant and $\frac{\partial\varepsilon}{\partial\eta}$ is its variation with strain; q is the acoustic wave number. A Fourier transform of Eq. (5) gives the calculated change of reflectivity in the time domain, and $\frac{\Delta\rho(t)}{\rho}$ is adjusted to the measured echoes to assess acoustic attenuation within the SiO_2 layer.

The details of the fitting procedure are presented in Ref. [41]. In the first place, the T-independent parameters entering the mismatch model are assessed by analyzing the shape of the first echo at 15 K for which the reflection losses dominate alone. In this respect, the surface-loading duration is found to be $\delta = 1.6$ ps and the metallic Al-film thickness $l = 18.8$ nm is evaluated. The acoustic impedance of the SiO_2 layer and the one of the substrate are set to their nominal value, whereas the Al-film acoustic impedance needs to be slightly adjusted. The best value is found to be 1.1 times the Al bulk value, possibly due to a partial oxydation of the film. Then, the time delay $\Delta t = d/v_g$ between successive echoes for each of the data (recorded at different temperatures) can be adjusted. Assuming $v_g = 5.95$ nm/ps the resulting values of d range from 283.2 to 285.0 nm in line with ellipsometry characterization. Since the thermal expansion is negligible, the $\Delta t(T)$ variations actually reflect sound velocity variations such that $\frac{\Delta v_g}{v_g} \lesssim 1\%$ over the whole investigated T range. Finally, all the above parameters being fixed, the attenuation-law parameters (α_0 and p) are obtained by fitting the three successive echoes to the model using a least squares method. Assuming only white noise over the signals, one obtains the standard deviation on parameters from which the 99 percent confidence interval may be derived. A typical signal at 45 K and its best fit are displayed in Fig. 3, exhibiting a very good agreement as shown by the small residual (bottom curve). Additional typical fitted curves for some selected T from 15 to 300 K are shown in Ref. [41]. The ability to carry out a simultaneous analysis of the first three echoes appears to be decisive in evaluating accurate

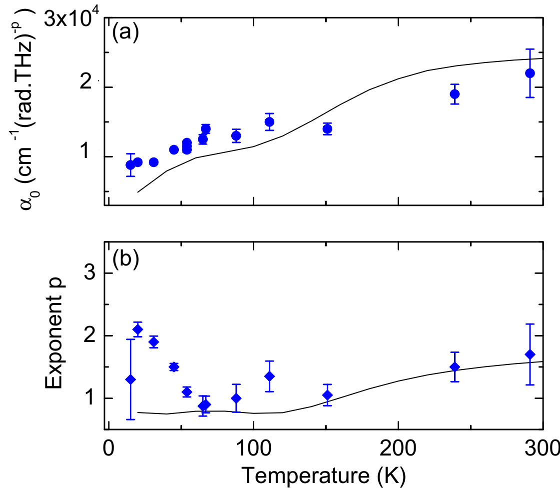

FIG. 4. Parameters α_0 and p entering the local effective law, $\alpha(\omega,T) = \alpha_0(T)\omega^{p(T)}$, for acoustic attenuation over the ω band of the pulse. The lines are expectation from a model combining damping from anharmonicity and 1.5 × TAR defects as explained in text.

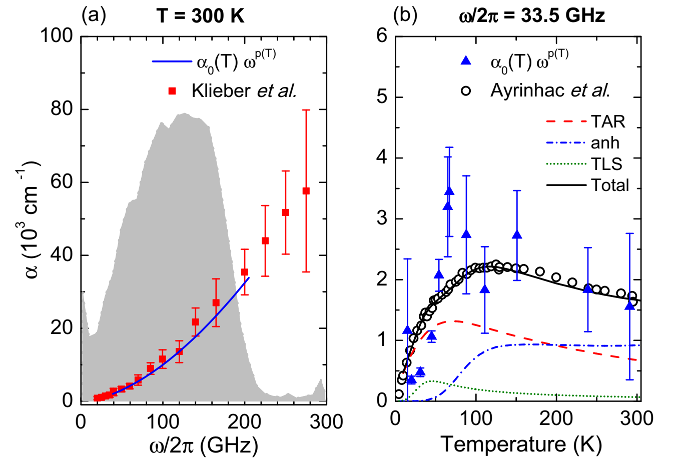

FIG. 5. (a) The acoustic attenuation rate as a function of frequency (–) derived from the α_0 and p parameters found at 300 K. The shaded area reminds the power spectrum of the acoustic pulse (first echo). Our finding overlaps the experimental determination by Klieber *et al.* [27] at room temperature (■). (b) The attenuation rates as a function of temperature derived at 33.5 GHz from the obtained $\alpha_0(T)$ and $p(T)$ parameters (▲). The values found in bulk v-SiO_2 from Brillouin scattering measurements at the same frequency (○) are shown as a reference [42]. The solid line is an adjustment of the Brillouin data made in Refs. [12,42], which is the sum of two main contributions, α_{TAR} and α_{anh} plus the tiny contribution α_{TLS} as explained in text.

attenuation parameters. Uncertainty on the attenuation values are calculated by propagating the confidence limits on the fitted parameters to the α values. The true uncertainty might be, however, somewhat larger due to the shortcomings of the model used for analyzing the echoes (Gaussian thermal strain generation in the Al film, monolayer of Al metal, perfect bounding at interfaces, etc.) which can hardly be quantified.

The above procedure cannot be applied to the *dryox* sample due to the weak acoustic contrast between v-SiO_2 and silicon. In that case, the second echo is poorly detected. Sound velocities $v(T)$ for the *dryox* SiO_2 layer are nevertheless determined evaluating the round-trip time for the first echo.

III. RESULTS AND DISCUSSIONS

A. Acoustic attenuation

The coefficients α_0 and p found upon cooling from 300 to 15 K are shown in Figs. 4(a) and 4(b). The prefactor α_0 decreases by a factor of about 2.5 emphasizing the lowering of the acoustic attenuation with decreasing T. The exponent p is found $\leqslant$2 at all temperatures which is consistent with relaxation processes. The resulting attenuation rates agree with the available ps acoustics results at room T for SiO_2 layers as illustrated in Fig. 5(a). We also plot in Fig. 5(b) the temperature dependence of the attenuation rate found at 33.5 GHz for which there exists a precise evaluation of $\alpha(T)$ in bulk v-SiO_2 from Brillouin scattering measurements [12,42] to serve as a reference. The data roughly overlap each other. Before we go any further, we outline in the following paragraph how the T dependence of the attenuation coefficient is currently explained. Note that attenuation coefficient is proportional to internal friction, *i.e.* the inverse of quality factor $Q^{-1} = \alpha v/\omega$, a form that will be used hereafter.

As already pointed out in the introduction, the hypersonic attenuation in v-SiO_2 mainly originates from the combined effects of TAR and anharmonicity. The phenomenological TAR model assumes the occurrence of structural defects that are represented by particles relaxing in an asymmetric double-well potential. It is widely recognized that sonic and ultrasonic damping in v-SiO_2 at T above 10 K is fully dominated by TAR defects [6,43,44]. The acoustic waves couple to the defects by a deformation potential γ, modifying their equilibrium population. Broad distributions for both energy barriers V and potential asymmetry Δ must be taken into account. The thermal rate of jumping from one state to the other (i.e., the inverse of relaxation time) for a given defect follows from Arrhenius expression,

$$\tau^{-1} = \frac{\tau_0^{-1}}{2}\exp\left(-\frac{V}{k_B T}\right)\cosh\left(\frac{\Delta}{2k_B T}\right), \tag{6}$$

where τ_0^{-1} is an attempt frequency. Integrating over the distribution, one obtains the expression

$$Q_{TAR}^{-1}(\omega,T) = \frac{\gamma^2}{\rho v^2 T}\int_{-\infty}^{\infty} d\Delta \int_0^{\infty} dV\, P(\Delta,V) \times \text{sech}^2\left(\frac{\Delta}{2k_B T}\right)\frac{\omega\tau}{1+\omega^2\tau^2}, \tag{7}$$

where $P(\Delta,V)d\Delta dV$ is the density of double well entities. A product of two distribution functions, a Gaussian in Δ, $f(\Delta) \propto \exp(-\Delta^2/2\Delta_C^2)$ of width Δ_C, times a modified Gaussian $g(V) \propto (V/V_0)^{-\zeta}\exp(-V^2/2V_0^2)$ of width V_0 is generally assumed (ζ is fixed to $\frac{1}{4}$) [45]. Introducing the latter in Eq. (7) leads to a functional form for Q_{TAR}^{-1} in which the total density of relaxing defects,

$$N \equiv \int_{-\infty}^{\infty} d\Delta \int_0^{\infty} dV\, P(\Delta,V), \tag{8}$$

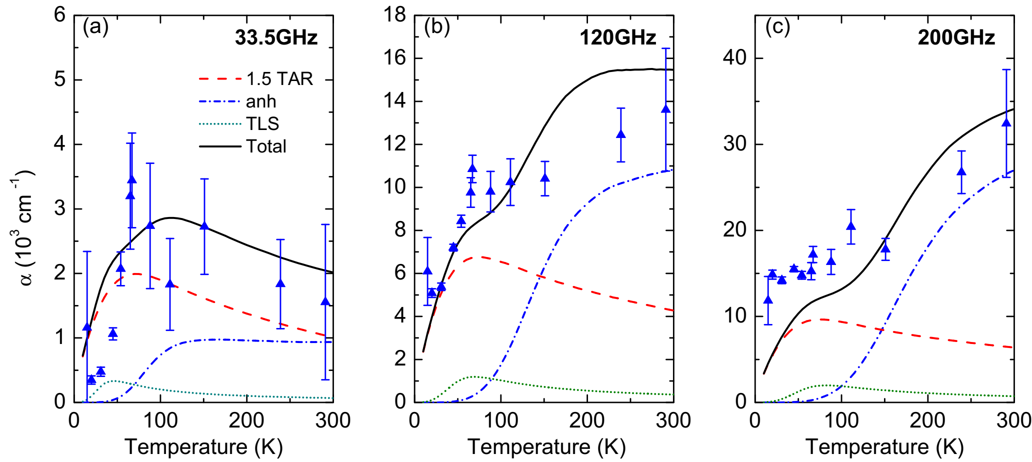

FIG. 6. Acoustic attenuation coefficient of energy obtained for the SiO_2 layer at (a) 33.5, (b) 120, and (c) 200 GHz in this work. The values are derived from the fitted parameters shown in Fig. 4 as explained in text. The solid curves are predictions combining two main contributions, $1.5 \times \alpha_{TAR}$ and α_{anh} plus the tiny contribution α_{TLS}. The α_{TAR} contribution in the SiO_2 layer is found nearly 1.5 times that in v-SiO_2 indicating more numerous relaxing defects.

enters as a prefactor. A dimensionless constant $\mathcal{C}_{TAR} \equiv \frac{N_g \gamma^2 N}{V_0 \rho v^2}$ is actually introduced for convenience (the constant of integration N_g equals 1.54 for $\zeta \simeq 0.25$). The handling of these equations is described in great details in Ref. [12]. The set of parameters $V_0/\Delta_C = 8.2$ with $V_0/k_B = 659$ K, $\tau_0 = 10^{-12.2}$ s, and $\mathcal{C}_{TAR} = 1.9 \times 10^{-3}$ was determined for v-SiO_2 by fitting internal friction and velocity dispersion results over sonic and ultrasonic domains. The same values apply to both LA and TA modes over four decades of frequency. The TAR contribution to $\alpha(T)$ extrapolated at the hypersonic frequency 33.5 GHz from these parameters is plotted as a dashed line in Fig. 5(b). A minor contribution to α from the tunneling systems (TLS) via relaxation channels so-called "incoherent tunneling" is also added from Ref. [12]. This contribution is shown in Fig. 5(b) as a thin doted black line.

The residual attenuation is interpreted as resulting from network viscosity [12,46]. The same approach as the one developed for crystals by Maris [11] is used for glasses. Phonons are treated as a gas in which anharmonic interactions lead to a mean thermal lifetime $\tau_{th}(T)$ between collisions [47]. This leads to the internal friction

$$Q^{-1}_{anh}(\omega,T) = A\frac{\omega\tau_{th}}{(1+\omega^2\tau_{th}^2)} \quad (9)$$

with

$$A(T) = \frac{C_v T v}{2\rho v_D^3}\bar{\gamma}_G{}^2. \quad (10)$$

Here, C_v is the specific heat per unit volume, v_D is the Debye velocity, and $\bar{\gamma}_G$ is an average Grüneisen parameter. The strongest assumptions in this development are the use of a single relaxation time $\tau_{th}(T)$ for thermal modes and a constant $\bar{\gamma}_G$. The anharmonic contribution to $\alpha(T)$ evaluated in Ref. [12] is plotted as a dot-dash line in Fig. 5(b) using $\bar{\gamma}_G = 3.8$ and the values of τ_{th} shown in Fig. 6(b) of Ref. [12].

As can be seen in Fig. 5(b), the attenuation found in the SiO_2 layer at 33.5 GHz displays a T-dependent behavior which follows the same trend as that of bulk v-SiO_2 at the same frequency. However, a detailed inspection yields to the following two observations:

(i) The attenuation in the SiO_2 layer exhibits a peak at about 50 K, just as that of bulk v-SiO_2 but it appears slightly larger and sharper. According to the TAR model, this would indicate the occurrence of more numerous relaxing defects in the layer than in the bulk sample.

(ii) Near room T, in contrast, the attenuation of the SiO_2 layer is mainly similar to that of bulk v-SiO_2 within the experimental errors. We therefore conclude that damping due to anharmonicity likely remains mostly identical for both materials. It also seems likely that phonon anharmonicity should not depend on the amount of relaxing defects, since they hardly affect the vibrational density of states.

Consequently, we plot as a dashed line in Fig. 6(a) the computed attenuation from TAR by arbitrarily multiplying the total density of relaxing defects by 1.5 (i.e., $1.5 \times \mathcal{C}_{TAR} = 2.85 \times 10^{-3}$) while keeping the double-wells parameters, V_0 and Δ_C, and the frequency attempt, τ_0, unchanged. By adding to the latter the contribution from anharmonicity found in v-SiO_2, one obtains the curve shown in Fig. 6(a) as a solid line. This almost fits to the data in the SiO_2 layer.

The same model (one and a half TAR-defects plus anharmonicity) approximately matches both the high frequency data at 120 and 200 GHz also shown in Fig. 6 without any additional assumptions. The two mechanisms are observed to clearly separate with increasing ω, the anharmonic part growing faster than the TAR one. Indeed, from Eq. (1), TAR attenuation near the maximum of its peak grows linearly with increasing ω, $\alpha_{TAR} \propto \omega$. In contrast, anharmonicity is in the regime $\omega\tau_{th} \ll 1$, so that $\alpha_{anh} \propto \omega^2$. All the above explains a posteriori the nontrivial T-dependent behavior found for the exponent of the power-law, used to represent the ω dependence of attenuation within the pulse and shown in Fig. 4(b). The calculated p from the model ($1.5 \times$ TAR plus anh.) is also shown in Fig. 4(b) as a solid line. Anharmonicity damping dominates the $p(T)$ variations near room T, while TAR mechanisms should prevail at low T. The deviation below 50 K might possibly be due to a small contribution of the

additional strong attenuation mechanism ($\alpha \propto \omega^4$) expected to come into play at high frequencies over anharmonicity as mentioned in the Introduction. Lastly, we should remark that the overall analysis further demonstrates the operability of the treatment proposed for network viscosity in Ref. [12]. Here we show that this remains suitable up to at least 200 GHz.

The number density of relaxing defects may be evaluated from the amplitude of TAR losses (i.e., from the $\mathcal{C}_{\rm TAR}$ value). For v-SiO_2, we get 0.64×10^{-12} Jm^{-3} for $\gamma^2 N$, the defects density multiplied by the square of the deformation potential. Taking γ of the order of 1 eV leads to about 1 defect per 650 SiO_2 molecules, close to the value 1/500 given in Ref. [48]. Microscopic models have been proposed to explain the origin of these relaxing entities [5]. The role of impurity defects (including that of OH group) was early excluded since they hardly affect acoustic loss amplitude [49]. The basic assumption is that owing to disorder, atoms or groups of atoms can occupy two or more equilibrium configurations. Applied pressure strongly affects TAR parameters [42,44]. It is further observed that TAR processes completely vanish in permanently densified silica glass upon 20% compaction [46,50,51]. This suggests that the relaxing entities are closely related to the largest interstitial voids within SiO_2 network (high-membered rings) which are removed by compaction [42]. The latter are manifested in the medium-range structure via the broad distribution of intertetrahedral bonding [52]. Compaction sharpens this distribution [53] thereby suppressing many double wells. Recent numerical works provide new insights into the nature of the relaxing entities in SiO_2 glass [54,55]. They would mainly involve rotations of the oxygen bonds over several connected tetrahedrons. These motions might indeed be promoted adjacent to the network vacancies. The enhancement of TAR absorption in deposited SiO_2 layer should thus indicate enhanced topological disorder that would promote the formation of numerous double-wells (we cannot, however, completely exclude either an enhanced value of γ possibly due to internal constraints in the SiO_2 layer). Anyway, this must be obviously related to layer preparation.

B. Velocity variations

The expectation for the velocity changes $(\delta v/v)_{\rm TAR}$ and $(\delta v/v)_{\rm anh}$ associated with the damping processes found in attenuation can be easily calculated [12]. Velocity dispersion being very low over the frequency spread of the strain pulse, we consider here the mean frequency of 120 GHz (v is incidentally assumed to be frequency independent in the fitting procedure). The reference value v_0 in the differential quantity $\frac{\delta v}{v} = \frac{v - v_0}{v_0}$ is taken as the low-T limit of v found by Brillouin scattering for v-SiO_2, namely $v_0 = 5.882$ nm ps^{-1}. Applying the Kramers-Kronig relation to Eq. (9) gives [12]

$$(\delta v/v)_{\rm anh} = -\frac{A}{2}\frac{1}{1+\omega^2\tau_{\rm th}^2}. \quad (11)$$

This produces the T dependence of $\delta v_{\rm anh}$ shown in Fig. 7 as dash-dot lines for 33.5 and 120 GHz. The $(\delta v/v)_{\rm anh}$ variations with T are controlled by $\tau_{\rm th}(T)$ variations. The knee in the curves around 150 K marks the region where $\omega\tau_{\rm th} \simeq 1$. It occurs at slightly larger T for 120 GHz than for 33.5 GHz. Below the knee, $\delta v_{\rm anh}(T)$ tends to zero since $\omega\tau_{\rm th} \gg 1$. Beyond it,

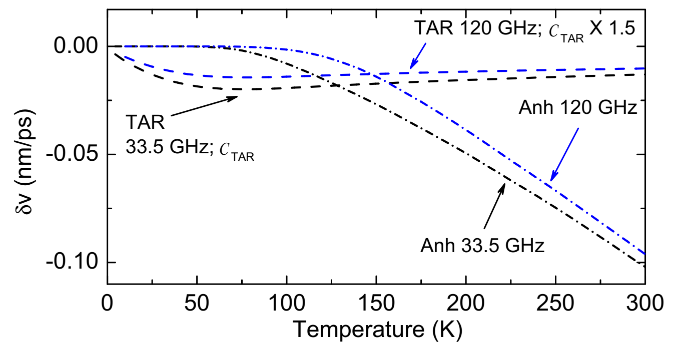

FIG. 7. The expectation for the $\delta v(T)$ patterns associated with TAR (dashed lines) and anharmonicity (dash-dot lines) mechanisms found in damping. The computation is at 120 GHz for the SiO_2 layer (blue lines) while it is at 33.5 GHz for bulk v-SiO_2 (black lines).

$\delta v_{\rm anh}$ becomes mostly controlled by the increase of $A(T)$ leading to an ω-independent linear decrease with T as $\omega\tau_{\rm th} \ll 1$.

The expected TAR contribution to velocity changes, $\delta v_{\rm TAR}$, is calculated using Eq. 1(b) of Ref. [12] with the parameters describing attenuation data found in the SiO_2 layer. Owing to the Kramers-Kronig relation, $(\delta v/v)_{\rm TAR}$ is expressed by an integral similar to Eq. (7), in which the last term is replaced by $-\frac{1}{2}\frac{1}{1+\omega^2\tau^2}$. This produces the T dependence of $\delta v_{\rm TAR}$ illustrated in Fig. 7. $\delta v_{\rm TAR}(T)$ should exhibit a dip nearly in coincidence with the maximum in internal friction $Q^{-1}_{\rm TAR}(T)$, as already discussed [12,44]. The absorption peak relates to those defects for which $\tau = \omega^{-1}$, τ following an Arrhenius law with temperature. Therefore, an increase in ω should result in an upper shift of the dip in $\delta v_{\rm TAR}(T)$. This should also involves a reduction of the dip amplitude as shown in Fig. 8(a) of Ref. [12] (due to the Kramers-Kronig transform, $\delta v_{\rm TAR}$ integrates over all defects with $\tau \leqslant \omega^{-1}$). The dip amplitude should remain anyway proportional to the total defects density N.

The $v(T)$ variations in the SiO_2 layer are obtained by two different methods: one is simply the usual round-trip time method, the other one is the fitting operation explained in Sec. II C. The values found for the sputtered SiO_2 layer are shown in Fig. 8(a) as triangle symbols. The data points with error bars are from the fitting method whereas the ones without are extra data from the round-trip time method. Accuracy on the absolute scale of $v(T)$ is limited by uncertainty on the layer thickness. Assuming 2 nm for the latter leads to about 0.04 nm/ps uncertainty on v. In contrast, accuracy on velocity changes $\delta v(T)$ is much higher since it is only governed by uncertainty on pump-probe delay (about $\Delta t \leqslant 0.1$ ps). This requires, however, that no fluctuation in layer thickness happens all along the experiment. The layer being possibly slightly wedge-shaped, a minor rescaling was necessary at each change in laser focusing spot location onto the sample. The $v(T)$ from Brillouin scattering in bulk v-SiO_2 are also displayed in Fig. 8 as circle (○) to serve as a reference [42]. We arbitrarily chose to make so that the velocity of the SiO_2 layer matches the one of bulk v-SiO_2, at low temperature.

The calculated total changes $\delta v_{\rm TAR} + \delta v_{\rm anh}$ discussed above should result in the occurrence of a small dip (at low T) followed by a linear decrease in the $v(T)$ data. In contrast, the $v(T)$ data exhibit a positive temperature coefficient as shown in Fig. 8(a) for both the SiO_2 layer (▲) and bulk v-SiO_2 (○). This is

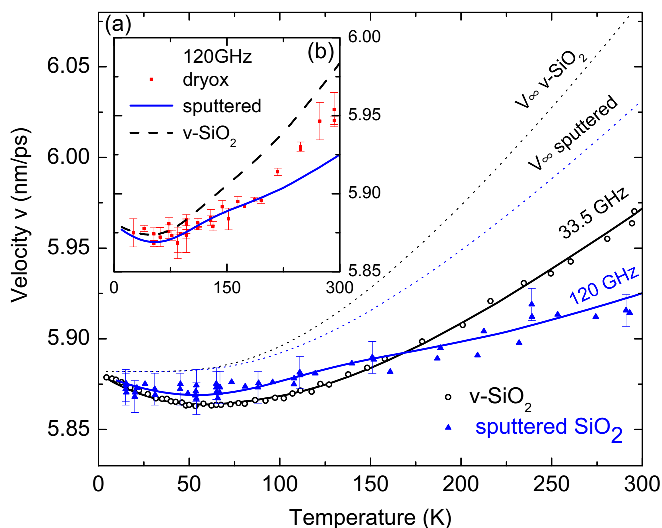

FIG. 8. (a) The $v(T)$ for the SiO_2 layer are shown as triangles (▲). The data points with error bars are from the fitting procedure, the ones without are extra data from the round-trip time method. The $v(T)$ values for bulk v-SiO_2 at 33.5 GHz shown as open dots (○) serve as a reference. The solid lines are our calculation $v = v_\infty + (\delta v_{TAR} + \delta v_{anh})$ using the appropriate δv_{TAR} and δv_{anh} values from Fig. 7 and the special purpose unrelaxed velocities v_∞ shown as dotted lines. (b) The inset shows the $v(T)$ values found for the *d*ryox SiO_2 layer from the round trip time method (●). They fall in between the $v(T)$ curves for the sputtered layer (lower blue curve) and for bulk v-SiO_2 computed at 120 GHz (upper black line).

because silica experiences well-known structural changes with T resulting in the occurrence of static $v(T)$ changes, which add to the dynamical ones. However, the calculated dynamical changes $(\delta v_{TAR} + \delta v_{anh})$ explain the low-T behavior of $v(T)$ data as shown in Fig. 8. The tiny dip in $v(T)$ near 60 K due to relaxing defects is actually partly buried into the experimental uncertainties. Nevertheless, a locally negative curvature of $v(T)$ is observed in the range 100 to 150 K resulting from the anharmonic losses. The latter result gives the earliest direct evidence of dissipative effects of relaxation via anharmonic interactions on sound velocity. The separate effects of thermally activated relaxations and anharmonicity are clearly demonstrated here in an experiment.

Subtracting both dynamical contributions from the $v(T)$ data, one obtains the so-called unrelaxed velocity $v_\infty = v - (\delta v_{TAR} + \delta v_{anh})$. This bare velocity which should be ω- and T-independent, is found to be a growing function of T in v-SiO_2 as discussed in Refs. [12,42]. The anomalous positive slope in $v(T)$ is in fact a peculiarity of all glasses with tetrahedral network as early reported [56–58]. This behavior has been attributed to T-dependent and reversible structural effects [59]. A progressive local polyamorphic transition associated with a redistribution of Si-O-Si bonds angles in configurations where they are more resilient, has been found in simulations [60,61]. The dotted lines in Fig. 8(a) are fits of $v_\infty(T)$ to an *ad hoc* Wachtman's equation for the SiO_2 layer and for v-SiO_2 (from Ref. [12]). The positive slope in $v_\infty(T)$ appears slightly reduced in the SiO_2 layer. It may be an additional indication that further small structural differences remain between the sputtered SiO_2-film and bulk vitreous silica.

We plot the $v(T)$ results for the *dryox* SiO_2 layer in Fig. 8(b). The values fall in between the ones for the sputtered SiO_2 layer (blue solid line) and the $v(T)$ curve computed at 120 GHz for bulk v-SiO_2 (black dashed line). A small dip at low-T (from TAR defects) followed by a slightly negative curvature (from anharmonic losses) is observed as well. Then the positive slope of $v_\infty(T)$ due to static v-changes takes over. The latter appears higher than that of the sputtered layer but still lower than that of bulk v-SiO_2. Reduced T coefficients for $v(T)$ have also been reported recently in CVD SiO_2 layers from picosecond acoustics [62].

Finally, one notes that an enhanced TAR-defects density is found in the sputtered layer while, in contrast, the slope of the static $v_\infty(T)$ changes is almost reduced by half. This provides further evidence that both anomalies likely have different origins. It was indeed, already observed that the anomalous T-induced stiffening of SiO_2 network keeps unchanged in permanently densified silica, while TAR defects are fully removed [46].

IV. SUMMARY AND OUTLOOKS

To summarize, the acoustical properties of an amorphous SiO_2 layer have been investigated by broadband ultrafast acoustic experiment for variable temperature between 20 to 300 K. A pulse-echo scheme is used, where a strain pulse is detected in an Al transducer after propagating back and forth through the SiO_2 layer. The attenuation of the acoustic pulse within the SiO_2 layer is evaluated at different temperature with the help of the effective attenuation law $\alpha(\omega,T) = \alpha_0(T)\omega^{p(T)}$ by fitting the successive echoes all at once. Such a law is inferred from the well established phenomenological models describing acoustic attenuation in v-SiO_2 at lower frequencies: coupling to thermally activated relaxation motions of structural defects and interaction with thermal vibrations.

A quantitative agreement is found between the values of $\alpha_0(T)$ and $p(T)$ identified in this work and a prediction combining TAR and anharmonicity mechanisms following Ref. [12]. The exponent is found to be $p \simeq 1$ near 50 K, while it goes up to $p \leqslant 2$ at room temperature emphasizing that TAR dominates the damping at low temperature while anharmonicity takes over at sufficiently high temperature. The acoustic absorption from TAR mechanisms in the SiO_2 layer is also found to be about one and a half larger than that in bulk v-SiO_2. A reasonable explanation would be that the rather *cold* deposition process used for preparation could generate a larger-than-usual quantity of relaxing defects, and thereby a higher TAR contribution, despite all our efforts to find the optimal growth conditions to sputter SiO_2 layers whose physical properties are as close as possible to those of bulk v-SiO_2. To our knowledge, only a SiO_2 film produced by thermal oxidation of Si at 1300 K (i.e., within the glass transition interval) has been found to exhibit internal friction identical to that in bulk v-SiO_2 [63].

Comparing this work to previous ps acoustics measurements, one notes that we have produced the first broadband measurement compatible with the available narrow-band ones (i.e. Refs. [26,27]). One also notes that the T dependence of acoustics properties in SiO_2 layers could be extracted in this work for the first time in contrast with the seminal work by Zhu

et al. [28] involving a broadband technique as well. Even if the susceptibility of the TAR-defect density to layer preparation might explain in part these discrepancies, it seems that the fitting procedure including an effective local law for $\alpha(\omega)$ has been crucial in retrieving accurate attenuation coefficients. It is noteworthy that our new results allow raising such issues. Ultrafast acoustics might provide potential for evaluating the TAR-defects concentration in amorphous layers, possibly opening the way to understand how to produce SiO_2 layers with low mechanical losses.

An immediate outlook of our work would be to finally search for the onset of the predicted ω^4 law over anharmonicity by moving to higher frequencies. Thinner metallic film could provide measurement up to 500 GHz. Other setups based on piezoelectric quantum wells [29] may reach the THz range close to the boson peak in v-SiO_2. Such experiments might provide the opportunity of directly probing the onset of the expected strong damping regime induced by disorder over anharmonicity on cooling. As the latter mechanism should be T-independent, the onset is expected to move down to lower frequency range as T is decreased reducing the anharmonicity damping.

ACKNOWLEDGMENTS

We thank Loïc Becerra, from the Institut des Nanosciences de Paris at UPMC, for the preparation of the thermally grown SiO_2 layer sample. This work has been supported by the Agence Nationale de la Recherche (Grant No. ANR-11-BS04-008-01, *GlassPhon*).

[1] S. Matsuda, M. Miura, T. Matsuda, M. Ueda, Y. Satoh, and K. Y. Hashimoto, IEEE Trans. Ultrason. Ferroelectr. Freq. Control **60**, 993 (2013).
[2] P. R. Saulson, Phys. Rev. D **42**, 2437 (1990).
[3] K. Numata, M. Ando, K. Yamamoto, S. Otsuka, and K. Tsubono, Phys. Rev. Lett. **91**, 260602 (2003).
[4] M. Granata, E. Saracco, N. Morgado, A. Cajgfinger, G. Cagnoli, J. Degallaix, V. Dolique, D. Forest, J. Franc, C. Michel, L. Pinard, and R. Flaminio, Phys. Rev. D **93**, 012007 (2016).
[5] O. L. Anderson and H. E. Bömmel, J. Am. Ceram. Soc. **38**, 125 (1955).
[6] J. Jäckle, L. Piché, W. Arnold, and S. Hunklinger, J. Non-Cryst. Solids **20**, 365 (1976).
[7] K. S. Gilroy and W. A. Phillips, Philos. Mag. **43**, 735 (1981).
[8] F. Travasso, P. Amico, L. Bosi, F. Cottone, A. Dari, L. Gammaitoni, H. Vocca, and F. Marchesoni, Europhys. Lett. **80**, 50008 (2007).
[9] J. Fabian and P. B. Allen, Phys. Rev. Lett. **82**, 1478 (1999).
[10] J.-Y. Duquesne and B. Perrin, Phys. Rev. B **68**, 134205 (2003).
[11] H. J. Maris, in *Physical Acoustics*, edited by W. P. Mason and R. N. Thurston (Academic Press, New York, 1971), Vol. VIII, pp. 279–345.
[12] R. Vacher, E. Courtens, and M. Foret, Phys. Rev. B **72**, 214205 (2005).
[13] J. Jäckle, Z. Phys. **257**, 212 (1972).
[14] L. Piché, R. Maynard, S. Hunklinger, and J. Jäckle, Phys. Rev. Lett. **32**, 1426 (1974).
[15] R. C. Zeller and R. O. Pohl, Phys. Rev. B **4**, 2029 (1971).
[16] B. Rufflé, M. Foret, E. Courtens, R. Vacher, and G. Monaco, Phys. Rev. Lett. **90**, 095502 (2003).
[17] B. Rufflé, G. Guimbretière, E. Courtens, R. Vacher, and G. Monaco, Phys. Rev. Lett. **96**, 045502 (2006).
[18] G. Monaco and V. M. Giordano, Proc. Natl. Acad. Sci. USA **106**, 3659 (2009).
[19] G. Baldi, V. M. Giordano, G. Monaco, and B. Ruta, Phys. Rev. Lett. **104**, 195501 (2010).
[20] C. Masciovecchio, G. Ruocco, F. Sette, P. Benassi, A. Cunsolo, M. Krisch, V. Mazzacurati, A. Mermet, G. Monaco, and R. Verbeni, Phys. Rev. B **55**, 8049 (1997).
[21] F. Sette, M. H. Krisch, C. Masciovecchio, G. Ruocco, and G. Monaco, Science **280**, 1550 (1998).
[22] R. Vacher, S. Ayrinhac, M. Foret, B. Rufflé, and E. Courtens, Phys. Rev. B **74**, 012203 (2006).
[23] C. Masciovecchio, A. Gessini, S. Di Fonzo, L. Comez, S. C. Santucci, and D. Fioretto, Phys. Rev. Lett. **92**, 247401 (2004).
[24] P. Benassi, S. Caponi, R. Eramo, A. Fontana, A. Giugni, M. Nardone, M. Sampoli, and G. Viliani, Phys. Rev. B **71**, 172201 (2005).
[25] B. Rufflé, E. Courtens, and M. Foret, Phys. Rev. B **84**, 132201 (2011).
[26] S. Ayrinhac, M. Foret, A. Devos, B. Rufflé, E. Courtens, and R. Vacher, Phys. Rev. B **83**, 014204 (2011).
[27] C. Klieber, E. Peronne, K. Katayama, J. Choi, M. Yamaguchi, T. Pezeril, and K. a. Nelson, Appl. Phys. Lett. **98**, 211908 (2011).
[28] T. C. Zhu, H. J. Maris, and J. Tauc, Phys. Rev. B **44**, 4281 (1991).
[29] Y.-C. Wen, S.-H. Guol, H.-P. Chen, J.-K. Sheu, and C.-K. Sun, Appl. Phys. Lett. **99**, 051913 (2011).
[30] B. Rufflé, D. A. Parshin, E. Courtens, and R. Vacher, Phys. Rev. Lett. **100**, 015501 (2008).
[31] A. Devos, M. Foret, S. Ayrinhac, P. Emery, and B. Rufflé, Phys. Rev. B **77**, 100201 (2008).
[32] H. Ogi, T. Shagawa, N. Nakamura, M. Hirao, H. Odaka, and N. Kihara, Phys. Rev. B **78**, 134204 (2008).
[33] P.-A. Mante, Y.-R. Huang, S.-C. Yang, T.-M. Liu, A. A. Maznev, J.-K. Sheu, and C.-K. Sun, Ultrasonics **56**, 52 (2015).
[34] E. S. K. Young, A. V. Akimov, R. P. Campion, A. J. Kent, and V. Gusev, Phys. Rev. B **86**, 155207 (2012).
[35] A. Barranco, F. Yubero, J. Cotrino, J. Espins, J. Benítez, T. Rojas, J. Allain, T. Girardeau, J. Rivire, and A. Gonzlez-Elipe, Thin Solid Films **396**, 9 (2001).
[36] J. Olivares, E. Wegmann, J. Capilla, E. Iborra, M. Clement, L. Vergara, and R. Aigner, IEEE Trans. Ultrason. Ferroelectr. Freq. Control **57**, 23 (2010).
[37] G. Tas and H. J. Maris, Phys. Rev. B **49**, 15046 (1994).
[38] O. B. Wright and V. Gusev, IEEE Trans. Ultrason. Ferroelectr. Freq. Control **42**, 331 (1995).
[39] B. Perrin, B. Bonello, J. C. Jeannet, and E. Romatet, Prog. Nat. Sci. **6**, 444 (1996).
[40] B. Perrin, B. Bonello, J.-C. Jeannet, and E. Romatet, Physica B **219-220**, 681 (1996).
[41] See Supplemental Material at http://link.aps.org/supplemental/10.1103/PhysRevB.96.174206 for more details about the implementation of the data analysis.

[42] S. Ayrinhac, B. Rufflé, M. Foret, H. Tran, S. Clément, R. Vialla, R. Vacher, J. C. Chervin, P. Munsch, and A. Polian, Phys. Rev. B **84**, 024201 (2011).
[43] W. A. Phillips, Rep. Prog. Phys. **50**, 1657 (1987).
[44] D. Tielbürger, R. Merz, R. Ehrenfels, and S. Hunklinger, Phys. Rev. B **45**, 2750 (1992).
[45] R. Keil, G. Kasper, and S. Hunklinger, J. Non-Cryst. Solids **164-166**, 1183 (1993).
[46] E. Rat, M. Foret, G. Massiera, R. Vialla, M. Arai, R. Vacher, and E. Courtens, Phys. Rev. B **72**, 214204 (2005).
[47] V. Gurevich, *Transport in Phonon Systems*, edited by V. Agranovich and A. Maradudin, Modern Problems in Condensed Matter Sciences Vol. 18 (North-Holland, Amsterdam Oxford New York Tokyo, 1986).
[48] S. Hunklinger and M. V. Schickfus, *Acoustic and Dielectric Properties of Glasses at Low Temperatures* (Springer-Verlag, Berlin, 1981) Chap. 6, pp. 79–105.
[49] R. E. Strakna, Phys. Rev. **123**, 2020 (1961).
[50] K. Döring, S. Rau, G. Weiss, J. Arndt, and S. Hunklinger, Phys. Lett. A **184**, 464 (1994).
[51] G. Weiss, A. Daum, M. Sohn, and J. Arndt, Physica B **219-220**, 290 (1996).
[52] C. Weigel, M. Foret, B. Hehlen, M. Kint, S. Clément, A. Polian, R. Vacher, and B. Rufflé, Phys. Rev. B **93**, 224303 (2016).
[53] R. J. Hemley, H. K. Mao, P. M. Bell, and B. O. Mysen, Phys. Rev. Lett. **57**, 747 (1986).
[54] R. Hamdan, J. P. Trinastic, and H. P. Cheng, J. Chem. Phys. **141**, 054501 (2014).
[55] C. R. Billman, J. P. Trinastic, D. J. Davis, R. Hamdan, and H.-P. Cheng, Phys. Rev. B **95**, 014109 (2017).
[56] J. T. Krause and C. R. Kurkjian, J. Am. Ceram. Soc. **51**, 226 (1968).
[57] R. Youngman, J. Kieffer, J. Bass, and L. Duffrene, J. Non-Cryst. Solids **222**, 190 (1997).
[58] A. Polian, D. Vo-Thanh, and P. Richet, Europhys. Lett. **57**, 375 (2002).
[59] A. G. Kalampounias, S. N. Yannopoulos, and G. N. Papatheodorou, J. Chem. Phys. **124**, 014504 (2006).
[60] L. Huang and J. Kieffer, Phys. Rev. B **69**, 224203 (2004).
[61] Y. Liang, C. R. Miranda, and S. Scandolo, Phys. Rev. B **75**, 024205 (2007).
[62] A. Nagakubo, H. Ogi, H. Ishida, M. Hirao, T. Yokoyama, and T. Nishihara, J. Appl. Phys. **118**, 014307 (2015).
[63] B. E. White and R. O. Pohl, Phys. Rev. Lett. **75**, 4437 (1995).